Anomalous Refraction of Acoustic Guided Waves in Solids with Geometrically Tapered Metasurfaces

Hongfei Zhu[1,*] and Fabio Semperlotti[1,2,†]
[1]Department of Aerospace and Mechanical Engineering, University of Notre Dame, Notre Dame, Indiana 46556, USA
[2]Ray W. Herrick Laboratories, School of Mechanical Engineering, Purdue University, West Lafayette, Indiana 47907, USA
(Received 1 March 2016; published 15 July 2016)

The concept of a metasurface opens new exciting directions to engineer the refraction properties in both optical and acoustic media. Metasurfaces are typically designed by assembling arrays of subwavelength anisotropic scatterers able to mold incoming wave fronts in rather unconventional ways. The concept of a metasurface was pioneered in photonics and later extended to acoustics while its application to the propagation of elastic waves in solids is still relatively unexplored. We investigate the design of acoustic metasurfaces to control elastic guided waves in thin-walled structural elements. These engineered discontinuities enable the anomalous refraction of guided wave modes according to the generalized Snell's law. The metasurfaces are made out of locally resonant toruslike tapers enabling an accurate phase shift of the incoming wave, which ultimately affects the refraction properties. We show that anomalous refraction can be achieved on transmitted antisymmetric modes (A_0) either when using a symmetric (S_0) or antisymmetric (A_0) incident wave, the former clearly involving mode conversion. The same metasurface design also allows achieving structure embedded planar focal lenses and phase masks for nonparaxial propagation.

DOI: 10.1103/PhysRevLett.117.034302

The concept of a metasurface has recently emerged as a powerful approach to effectively manipulate wavelike fields while breaking the dependence on the propagation length. Metasurfaces [1] were first studied in optics and implemented via optical antennas [2,3] or microwave metamaterials [4,5] in the context of light propagation across phase discontinuities. The generalized Snell's law (GSL) was introduced in order to predict the anomalous propagation across material interfaces characterized by a phase gradient [2]. Optical devices able to achieve unconventional wave front manipulation capabilities have been theoretically predicted and experimentally demonstrated. A few remarkable examples concern bending light in arbitrary shapes [3,6], the conversion of propagating into surface modes [7], and the development of ultrathin lenses [8,9]. Shortly after the introduction of metasurfaces in optics, the concept was adopted in acoustics with the intent to create subwavelength acoustic devices. To date, the most notable design of an acoustic metasurface is based on the labyrinthine [10–14], or space-coiling, unit. Anomalous reflection and refraction have been both numerically [15,16] and experimentally [17–22] demonstrated with labyrinthine units based on phase discontinuities. For completeness, we note that acoustic metasurfaces based on impedance discontinuities (as opposed to phase discontinuities) have also been theoretically demonstrated [23,24].

Despite much progress in the development of these subwavelength designs in both optics and acoustics, the extension of this concept to the control of elastic waves in solids has not received much attention other than for a few studies on elastic waveguides with metamaterial inserts [25–27]. The ability to extend the concept of a metasurface to a solid could provide novel and important functionalities for structural acoustic waveguides while drastically expanding their range of application. Applications would range from acoustic lenses for ultrasonic imaging and surgery, to the dynamic tailoring of structural components for effective vibration and noise control, to passive energy management for effective harvesting. In this Letter, we show both numerically and experimentally the possibility to successfully design acoustic metasurfaces fully embedded in structural waveguides and able to reliably achieve anomalous refraction. The metasurface design is based on the use of geometric tapers recently introduced by Zhu [28] in the context of thin-walled acoustic metamaterials. Previous results have shown that a periodic lattice of these geometric inhomogeneities can provide a high level of control of the propagation parameters. At the same time, this design drastically reduces the fabrication complexity of traditional metamaterial systems based on a multimaterial approach [29–31].

According to the GSL [2], the direction of anomalous refraction is related to the direction of the incident planar wave front as follows:

$$\frac{\sin(\theta_t)}{\lambda_t} - \frac{\sin(\theta_i)}{\lambda_i} = \frac{1}{2\pi}\frac{d\phi}{dy}. \tag{1}$$

Equation (1) implies that the refracted beam can have an arbitrary direction, provided that a suitable constant phase gradient ($d\phi/dy$) can be produced along the interface. In order to design metasurfaces that can effectively steer the transmitted guided wave, it is necessary to achieve a spatial gradient profile able to cover the entire 2π phase range. This condition translates into constraints on the frequency response of the different scatterers. In particular, it requires

that every scatterer achieve a full 2π phase change while simultaneously maximizing the amplitude of the transmitted wave (i.e., reducing the backscattering). Mode conversion is one of the most characteristic traits of acoustic wave propagation in solids as compared to fluids or gases. In the present study, we show the possibility to achieve anomalous refraction for the A_0 antisymmetric transmitted mode by illuminating the metasurface with either a symmetric S_0 or an A_0 incident mode. We will discuss the design for the S_0 excitation in detail while observing that the operating mechanism and the design strategy apply similarly to the A_0 mode.

The proposed approach synthesizes the metasurface based on periodic arrays of elements whose individual unit consists of a geometrically inhomogeneous cell combined with a resonating core. The fundamental building block of the metasurface [Fig. 1(a)] is a square unit (side length $L = 4$ cm) having an embedded elliptic toruslike taper and a (resonating) center mass whose value can be tuned by controlling its thickness. The xz cross section of a typical unit is presented in Fig. 1(b), where t, a, b, r, and h are the defining geometric parameters. In this study, we mostly concentrated on the parameter h that is the thickness of the tunable center mass, which affects more directly the local resonance of the building block design, combined with different taper profiles (details provided in the Supplemental Material [32]). In order to evaluate the frequency response of the different units, we numerically calculated the transmitted A_0 mode resulting from an incident S_0 plane wave impinging normally on the metasurface. The phase and amplitude response were extracted from displacement data collected in the far field. The frequency response characterization for each unit was performed on individual 3D striplike models with a single embedded unit and periodic boundary conditions applied on the top and bottom boundaries, as shown in Fig. 1(c) (top). For the sake of clarity and to facilitate the comparison between different units, we selected a specific frequency of actuation ($f = 20.1$ kHz), which was used throughout the numerical simulations. This frequency corresponded to a wavelength of the S_0 mode $\lambda_{S_0} \approx 27$ cm $\sim 6.75L$ and of the A_0 mode $\lambda_{A_0} \approx 5.9$ cm $\sim 1.5L$ for an 8 mm thick aluminum plate as considered in the numerical results.

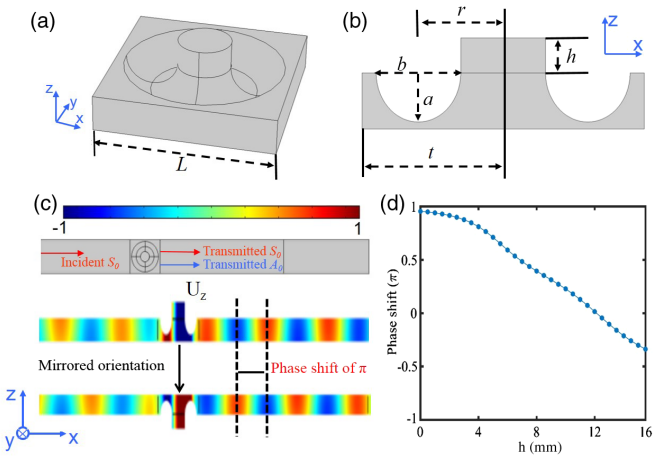

FIG. 1. Schematic of the (a) elliptic toruslike tapered unit and of (b) its xz plane cross section showing the main geometric parameters. (c) Full field results illustrating the π phase shift occurring on the transmitted (mode converted) A_0 mode generated by a normally incident S_0 mode when the same taper geometry is mirrored about the neutral plane. (d) The phase shift response of a single unit at $f = 20.1$ kHz as a function of the thickness of the center mass (which results in a resonance frequency shift).

In order to reduce the design complexity while still achieving phase shifts covering the entire 2π range, we recognized that symmetry conditions could be exploited for the S_0 actuation mode. Consider a pair of exactly identical tapered units; a π phase shift difference in the transmitted and mode-converted A_0 wave can be achieved if the unit's orientation is mirrored with respect to the neutral plane [see Fig. 1(c)]; this is a direct result of enforcing the continuity of the displacements in the z direction at the interface between the flat plate and the unit cell. These design considerations were confirmed by the finite element simulations [Fig. 1(c)] that show the out-of-plane displacement field associated with the transmitted A_0 mode. The results of the two models, corresponding to the same taper geometry with mirror symmetry, clearly confirm the phase shift difference of π. Hence, the use of the mirrored geometry allows reducing the design complexity because the individual units are required to cover only a phase range of π, while the remaining (π) shift can be obtained by a mirroring operation. In fact, the phase shift obtained by varying the thickness h of the attached mass (up to twice the plate thickness) already produces phase shifts largely in excess of π [Fig. 1(d)]. These results suggest that a metasurface with a given phase gradient can be designed by carefully selecting unit cells having the desired transmission properties (see Fig. 1 of Supplemental Material [32]).

In the following, we explore the possibility of achieving different wave manipulation effects by exploiting embedded acoustic metasurfaces based on combinations of different fundamental units. In particular, we will show two mechanisms that could prove critical for the development of future ultracompact acoustic devices: (1) a flat ultrathin lens, and (2) a phase mask for nonparaxial propagation.

To illustrate the anomalous refraction phenomenon, which is the fundamental physical mechanism at the basis of all the other designs, we assembled a metasurface based on a one-dimensional periodic array of supercells. The individual supercell was built using different units properly selected to achieve a prescribed spatial phase gradient. The units were fully integrated in the host structure consisting of an 8 mm thick aluminum plate, as shown in Fig. 2(a). The expected refraction angle $\theta_t = \arcsin[(\lambda_t \sin(\theta_i)/\lambda_i) + (\lambda_t/2\pi)(d\phi/dy)]$ was predicted according to the GSL. For the numerical investigation, we built a supercell based on different units (see the Supplemental Material [32]). The three different configurations provided a phase shift of $d\phi = \pi/3$, $d\phi = \pi/2$, $d\phi = 2\pi/3$ along the interface. The metasurface was excited by a normally incident S_0 Gaussian beam from left to right. Figures 2(b) and 2(c) show the transmitted A_0

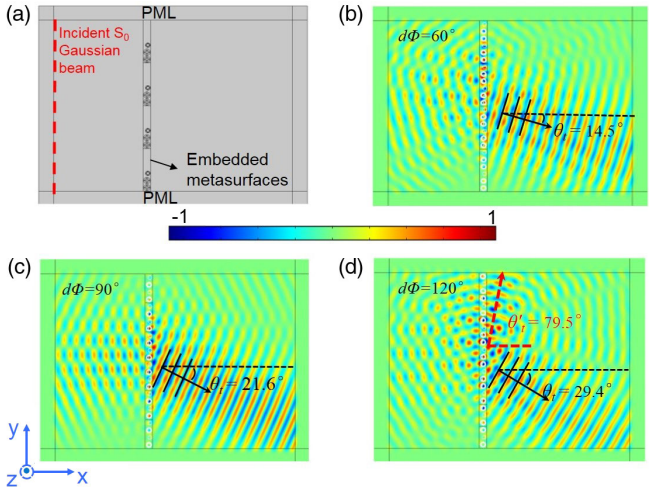

FIG. 2. (a) Schematic of the thin plate with the embedded metasurface. An S_0 Gaussian beam with normal incidence was used as the external excitation. Perfectly matched layers surrounding the domain of simulation and used to minimize boundary reflections. Panels (b)–(d) show the transmitted (mode-converted) A_0 wave field for three metasurfaces having a different value of the spatial gradient obtained by numerical finite element method simulations.

mode for the different values of the phase gradient. Note that in all of the following numerical results the A_0 wave fields are always plotted in terms of out-of-plane displacements (z component) at the neutral plane of the plate, which allows for an effective separation of the S_0 and A_0 modes. The numerical results for every configuration show clear evidence of the anomalous refraction phenomenon. The superimposed black arrows in Figs. 2(b)–2(d) indicate the analytical prediction according to the GSL, that is, $\theta_t^{(60°)} \approx 14.5°$, $\theta_t^{(90°)} \approx 21.6°$, and $\theta_t^{(120°)} \approx 29.4°$. For comparison, the angles of refraction were also extracted from the full field numerical simulations, which provided the following values: 15.25°, 22.16°, and 28.65°.

Only in the case of the strongest spatial gradient [Fig. 2(d)] was a visible portion of the incident beam converted into a second refracted beam. This can be explained by the existence of a critical value for the phase discretization, that is, the value of $d\phi$ between adjacent units. It can be shown that, beyond a certain value of $d\phi$ two possible propagating wave solutions can be supported by the same metasurface configuration. The refraction angle of the second refracted beam can be determined by $\theta_t' = \arcsin[(\lambda/2\pi)(-4/3\pi/dy)] = -79.5°$, which is in good agreement with the numerical simulation [dashed red arrow in Fig. 2(d)]. In our current configuration, the critical value for $d\phi$ can be calculated as $d\phi_c = 2\pi - (2\pi dx/\lambda) = 0.644\pi$. Aside from these additional considerations, the results clearly illustrate that the proposed metasurface design is able to induce strong anomalous refraction on the A_0-converted Lamb modes.

In order to apply this methodology to design a flat focal lens, a hyperbolic phase profile must be programmed into the metasurface [Fig. 3(a)]. For a given focal length f, the phase shift $\phi(y)$ profile is provided by

$$\phi(y) = \vec{k} \cdot \overline{SP} = \frac{2\pi}{\lambda}(\sqrt{f^2 + y^2} - f), \qquad (2)$$

where $\vec{k}$ is the wave vector, $\overline{SP}$ is the distance to compensate for in order to achieve a hyperbolic profile, and f is the focal length (that is the distance $\overline{OF}$).

To show the capabilities of the metasurface, we designed a lens having a focal length $f = 70$ cm. The corresponding phase profile needed to achieve this performance was obtained according to Eq. (2) and is plotted in Fig. 3(a) (blue curve). The corresponding discrete phase profile (red dots) is plotted in Fig. 3(a) and the lens can be readily constructed by selecting units that match the requested phase shift (see the Supplemental Material [32]). Note that the lens was designed with the intent to use a normally incident S_0 excitation and to achieve a focal point in the transmitted A_0 (converted) mode. Figure 3(b) shows the spatial distribution of the intensity of the transmitted wave field $|A|^2$ after the metasurface. A very narrow focal point is achieved at $x \approx 68$ cm, which is within a 3% error from the target location ($f = 70$ cm). Further analyses of the performance of the acoustic lens can be found in the Supplemental Material [32].

Our metasurface design can also be exploited to create phase masks (essentially, acoustic analog filters) to generate self-accelerating acoustic beams that propagate along an arbitrary convex trajectory, a mechanism also known as nonparaxial propagation. We design the metasurface to perform as a phase mask able to convert an incident wave into a nonparaxial beam. Based on caustic theory [33–35], the continuous phase profile along the metasurface can be synthesized in order to achieve an arbitrary convex trajectory of the transmitted acoustic beam. Once the continuous phase profile is available, its discrete approximation can be easily obtained by selecting basic unit cells according to a procedure analogous to that described for the flat lens. The detailed description to construct the phase profile $\phi(y_0)$ for an arbitrary convex trajectory $y = f(x)$ can be found in the Supplemental Material [32].

The ability of the metasurface to generate nonparaxial beam propagation is numerically shown by means of two different examples: (1) a half circular and (2) a parabolic trajectory. The half circular path having radius

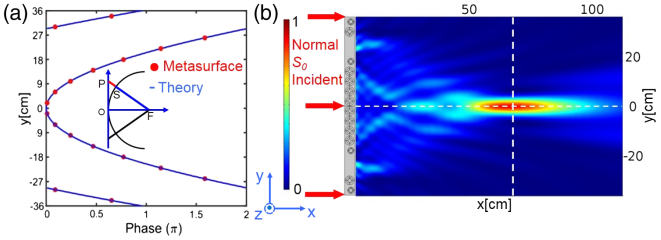

FIG. 3. Design and numerical evaluation of a flat focal lens based on the embedded metasurface concept. Panel (a) shows the continuous hyperbolic phase profile (blue curves) and the corresponding discrete phase profile (red dots) effectively implemented in the metasurface. The inset illustrates schematically how to synthesize the phase profile. (b) The intensity distribution $|A|^2$ of the transmitted A_0 wave field after the flat focal lens.

r and centered at $(r,0)$ is described by the equation $y=f(x)=\sqrt{r^2-(r-x)^2}$. The desired phase profile is $\phi(y_0)=-k_0[y_0-2r\arctan(y_0/r)]$. Concerning the parabolic trajectory $y=f(x)=a\sqrt{x}$, the desired phase profile is $\phi(y_0)=-k_0[-\ln(y_0+\sqrt{y_0^2+(a^2/4)^2})]a^2/4$. For the numerical example, the parameters r and a controlling the curvatures of the paths were selected as $r=0.2m$ and $a=\sqrt{0.32}$, in order to guarantee the smoothness of the discrete phase profile. The resulting metasurfaces were embedded in the host 8 mm thick plate and excited by an incident S_0 plane wave. The numerical results are provided in Figs. 4(a) and 4(b) in terms of the full displacement fields associated with the transmitted (mode-converted) A_0 wave. In both cases, the results show good agreements between the target and the calculated trajectories. Clearly, the circular trajectory exhibits a larger error in the far quarter of the path due to the finite length of the metasurface.

The design approach described above was based on mode conversion, which is a useful but not strictly necessary mechanism to build the metasurface. To substantiate this statement we explored the design of a metasurface able to operate on a nonconverted mode, that is, as an example, on transmitted A_0 modes generated by incident A_0 modes. The results (summarized in Fig. 2 of the Supplemental Material [32]) showed that a comparable anomalous refraction performance can be achieved also for this alternative design.

In order to validate the concept of a geometrically tailored acoustic metasurface, we performed a set of experimental investigations. Three different test beds were built so to validate the anomalous refraction under the (1) mode converted (S_0-A_0) and (2) direct (A_0-A_0) actuation mode, and (3) parabolic nonparaxial propagation. The experimental test beds consisted of a thin flat aluminum plate having a single embedded metasurface [see Fig. 5(a); the enlargement of the white box shows the fundamental supercell]. The plate thickness was reduced to 4.06 mm and the target operating frequency was set to 50.1 kHz. The toruslike tapers were computer numerical control machined while the center masses were successively glued on the taper. The experimental sample was mounted in an aluminum frame and a viscoelastic tape was glued on the edges in order to minimize boundary reflections. The out-of-plane response of the plate

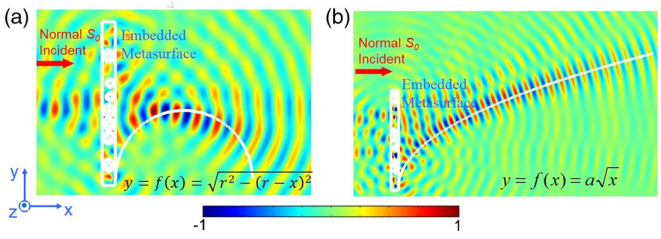

FIG. 4. Nonparaxial self-accelerating acoustic beam achievable by a metasurface phase mask. Numerical simulations illustrated that both designs can successfully achieve nonparaxial beams on the transmitted A_0 mode under normal S_0 excitation for either (a) a half circular trajectory path or (b) a parabolic trajectory. The white solid lines in each plot represent the target trajectory.

was acquired by using a Polytec PSV-500 laser scanning vibrometer.

The full field experimental measurements for the two anomalous refraction cases are shown in Figs. 5(b) and 5(c). An array of microfiber composite (MFC) patches [Fig. 5(a)] was surface bonded on the plate and simultaneously actuated to generate a quasi A_0 planar incident wave. Similarly, for the S_0 actuation an identical array of MFCs was bonded symmetrically on the other side of the plate and drive in phase. In both cases, the excitation was a 25-count wave burst with a 50.1 kHz center frequency. For the A_0-A_0 actuation [Fig. 5(c)] the metasurface was assembled based on periodic supercells providing a phase increment of $(2\pi/3)$ between adjacent units, while for the S_0-A_0 case [Fig. 5(b)] a phase increment of $(\pi/2)$ was used. Note that in these two cases the dimensions of the subunits are different and correspond to analytical refraction angles equal to $\theta_t^{S_0-A_0}=\arcsin[(\lambda_t/2\pi)(\pi/2/0.016)]=22.5°$ and $\theta_t^{A_0-A_0}=\arcsin[(\lambda_t/2\pi)(2\pi/3/0.02)]=24.1°$. The experimentally observed angles are 22.8° and 21.6°, correspondingly, which are in good agreement with both the numerical results and the analytical predictions. The transmittance is approximately 0.54 for the direct A_0-A_0 actuation mode (measured by the ratios of the averaged peak value of the incident and refracted wave fronts). For the S_0-A_0 mode, the incident S_0 wave field was not measured but, based on the numerical simulations, a transmittance (S_0 to A_0) around 0.528 was estimated. Figure 5(d) shows the experimental results for the nonparaxial propagation under the S_0-A_0 operating mode. The white solid line represents the target trajectory [that is, $y=f(x)=\sqrt{0.125}\sqrt{x}$] and highlights the good agreement between the analytical prediction and the experimentally

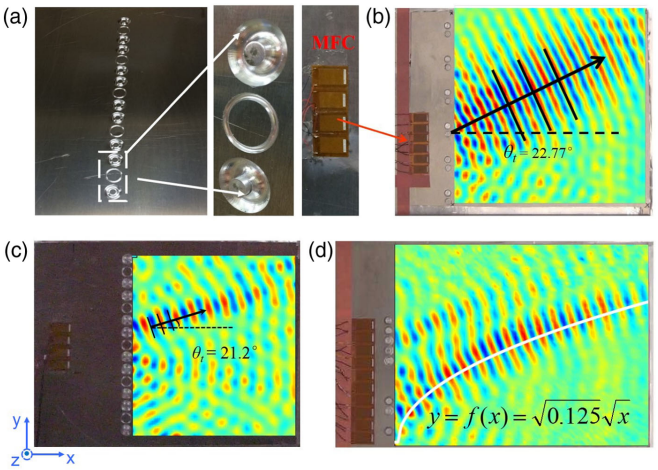

FIG. 5. Experimental setup and results. (a) Side view of the embedded metasurface on a 4 mm thick aluminum plate. The enlargement shows an example of the fundamental supercell from which the metasurface is assembled. An array of MFC patches was surface bonded to generate the ultrasonic excitation. The measured transmitted A_0 wave fields (out-of-plane component) are shown in (b), (c), and (d) for the S_0-A_0 anomalous refraction, the A_0-A_0 anomalous refraction, and the nonparaxial propagation cases.

generated acoustic beam. The numerical simulations corresponding to the experimental configurations are provided in Fig. 5 of the Supplemental Material [32].

In conclusion, we have presented and experimentally demonstrated the design of structure-embedded acoustic metasurfaces, which can be exploited to produce a variety of unconventional wave manipulation effects in structural waveguides. Numerical and experimental results were in excellent agreement showing the robustness of the approach and the high level of performance achievable with the tapered design. Acoustic wave control was shown for both same-mode and mode-converted transmitted waves. Applications of the metasurface to acoustic planar focal lenses and phase masks for nonparaxial propagation were also successfully investigated by numerical simulations and showed an outstanding potential for wave control and device fabrication. The tapers are extremely easy to fabricate and eliminate completely the need for the multimaterial interfaces typical of the more traditional acoustic metamaterial design. This is a critical aspect to achieve scalability and to transfer metamaterial concepts to structural members with load-bearing capabilities.

The authors gratefully acknowledge the financial support of the Air Force Office of Scientific Research (Grant No. YIP FA9550-15-1-0133) under the supervision of Dr. James Fillerup.

*Hongfei.Zhu.44@nd.edu
†To whom all correspondence should be addressed.
fsemperl@purdue.edu

[1] N. Yu and F. Capasso, Flat optics with designer metasurfaces, Nat. Mater. **13**, 139 (2014).
[2] N. Yu, P. Genevet, M. A. Kats, F. Aieta, J.-P. Tetienne, F. Capasso, and Z. Gaburro, Light propagation with phase discontinuities: generalized laws of reflection and refraction, Science **334**, 333 (2011).
[3] X. Ni, N. K. Emani, A. V. Kildishev, A. Boltasseva, and V. M. Shalaev, Broadband light bending with plasmonic nanoantennas, Science **335**, 427 (2012).
[4] N. K. Grady, J. E. Heyes, D. R. Chowdhury, Y. Zeng, M. T. Reiten, A. K. Azad, A. J. Taylor, D. A. R. Dalvit, and H.-T. Chen, Terahertz metamaterials for linear polarization conversion and anomalous refraction, Science **340**, 1304 (2013).
[5] C. Pfeiffer and A. Grbic, Metamaterial Huygens' Surfaces: Tailoring Wave Fronts with Reflectionless Sheets, Phys. Rev. Lett. **110**, 197401 (2013).
[6] L. Huang, X. Chen, H. Muhlenbernd, G. Li, B. Bai, Q. Tan, G. Jin, T. Zentgraf, and S. Zhang, Dispersionless phase discontinuities for controlling light propagation, Nano Lett. **12**, 5750 (2012).
[7] S. Sun, Q. He, S. Xiao, Q. Xu, X. Li, and L. Zhou, Gradient-index meta-surfaces as a bridge linking propagating waves and surface waves, Nat. Mater. **11**, 426 (2012).
[8] F. Aieta, P. Genevet, M. A. Kats, N. Yu, R. Blanchard, Z. Gaburro, and F. Capasso, Aberration-free ultrathin flat lenses and axicons at telecom wavelengths based on plasmonic metasurfaces, Nano Lett. **12**, 4932 (2012).
[9] M. Kang, T. Feng, H.-T. Wang, and J. Li, Wave front engineering from an array of thin aperture antennas, Opt. Express **20**, 15882 (2012).
[10] Z. Liang and J. Li, Extreme Acoustic Metamaterial by Coiling Up Space, Phys. Rev. Lett. **108**, 114301 (2012).
[11] Y. Li, B. Liang, X. Tao, X.-f. Zhu, X.-y. Zou, and J.-c. Cheng, Acoustic focusing by coiling up space, Appl. Phys. Lett. **101**, 233508 (2012).
[12] Z. Liang, T. Feng, S. Lok, F. Liu, K. B. Ng, C. H. Chan, J. Wang, S. Han, S. Lee, and J. Li, Space-coiling metamaterials with double negativity and conical dispersion, Sci. Rep. **3**, 1614 (2013).
[13] Y. Xie, B.-I. Popa, L. Zigoneanu, and S. A. Cummer, Measurement of a Broadband Negative Index with Space-Coiling Acoustic Metamaterials, Phys. Rev. Lett. **110**, 175501 (2013).
[14] T. Frenzel, J. David Brehm, T. Bckmann, R. Schittny, M. Kadic, and M. Wegener, Three-dimensional labyrinthine acoustic metamaterials, Appl. Phys. Lett. **103**, 061907 (2013).
[15] J. Mei and Y. Wu, Controllable transmission and total reflection through an impedance-matched acoustic metasurface, New J. Phys. **16**, 123007 (2014).
[16] Y. Li, B. Liang, Z. Gu, X. Zou, and J. Cheng, Reflected wavefront manipulation based on ultrathin planar acoustic metasurfaces, Sci. Rep. **3**, 2546 (2013).
[17] Y. Li, X. Jiang, R. Q. Li, B. Liang, X. Y. Zou, L. L. Yin, and J. C. Cheng, Experimental Realization of Full Control of Reflected Waves with Subwavelength Acoustic Metasurfaces, Phys. Rev. Applied **2**, 064002 (2014).
[18] Y. Xie, W. Wang, H. Chen, A. Konneker, B.-I. Popa, and S. A. Cummer, Wavefront modulation and subwavelength diffractive acoustics with an acoustic metasurface, Nat. Commun. **5**, 5553 (2014).
[19] K. Tang, C. Qiu, M. Ke, J. Lu, Y. Ye, and Z. Liu, Anomalous refraction of airborne sound through ultrathin metasurfaces, Sci. Rep. **4**, 6517 (2014).
[20] Y. Zhu, X. Zou, R. Li, X. Jiang, J. Tu, B. Liang, and J.-C. Cheng, Dispersionless manipulation of reflected acoustic wavefront by subwavelength corrugated surface, Sci. Rep. **5**, 10966 (2015).
[21] B. Yuan, Y. Cheng, and X. Liu, Conversion of sound radiation pattern via gradient acoustic metasurface with space-coiling structure, Appl. Phys. Express **8**, 027301 (2015).
[22] K. Tang, C. Qiu, J. Lu, M. Ke, and Z. Liu, Focusing and directional beaming effects of airborne sound through a planar lens with zigzag slits, J. Appl. Phys. **117**, 024503 (2015).
[23] J. Zhao, B. Li, Z. Chen, and C. W. Qiu, Manipulating acoustic wavefront by inhomogeneous impedance and steerable extraordinary reflection, Sci. Rep. **3**, 2537 (2013).
[24] J. Zhao, B. Li, Z. N. Chen, and C.-W. Qiu, Redirection of sound waves using acoustic metasurface, Appl. Phys. Lett. **103**, 151604 (2013).
[25] X. Yan, R. Zhu, G. Huang, and F.-G. Yuan, Focusing guided waves using surface bonded elastic metamaterials, Appl. Phys. Lett. **103**, 121901 (2013).
[26] R. Zhu, X. Liu, G. K. Hu, C. Sun, and G. Huang, Negative refraction of elastic waves at the deep-subwavelength scale in a single-phase metamaterial, Nat. Commun. **5**, 5510 (2014).
[27] R. Zhu, X. Liu, and G. Huang, Study of anomalous wave propagation and reflection in semi-infinite elastic metamaterials, Wave Motion **55**, 73 (2015).

[28] H. Zhu and F. Semperlotti, Phononic thin plates with embedded acoustic black holes, Phys. Rev. B **91**, 104304 (2015).
[29] Y. Wu, Y. Lai, and Z.-Q. Zhang, Elastic Metamaterials with Simultaneously Negative Effective Shear Modulus and Mass Density, Phys. Rev. Lett. **107**, 105506 (2011).
[30] Y. Lai, Y. Wu, P. Sheng, and Z.-Q. Zhang, Hybrid elastic solids, Nat. Mater. **10**, 620 (2011).
[31] X. N. Liu, G. K. Hu, G. L. Huang, and C. T. Sun, An elastic metamaterial with simultaneously negative mass density and bulk modulus, Appl. Phys. Lett. **98**, 251907 (2011).
[32] See Supplemental Material at http://link.aps.org/supplemental/10.1103/PhysRevLett.117.034302 for analytical solutions and additional numerical and experimental results.
[33] E. Greenfield, M. Segev, W. Walasik, and O. Raz, Accelerating Light Beams along Arbitrary Convex Trajectories, Phys. Rev. Lett. **106**, 213902 (2011).
[34] S. Zhao, Y. Hu, J. Lu, X. Qiu, J. Cheng, and I. Burnett, Delivering sound energy along an arbitrary convex trajectory, Sci. Rep. **4**, 6628 (2014).
[35] L. Froehly, F. Courvoisier, A. Mathis, M. Jacquot, L. Furfaro, R. Giust, P. A. Lacourt, and J. M. Dudley, Arbitrary accelerating micron-scale caustic beams in two and three dimensions, Opt. Express **19**, 16455 (2011).